

Section 1

Assimilation of atmospheric and land observations.

Data impact and sensitivity studies.

Methodological advances.

Dynamically Weighted Hybrid Gain Data Assimilation

Helena Barbieri de Azevedo^{1,2}, Luis Gustavo Goncalves de Goncalves², Eugenia Kalnay³,
Matthew Wespetal³

¹ helenabdeazevedo@gmail.com

² Instituto Nacional de Pesquisas Espaciais, Cachoeira Paulista - SP, Brasil

³ University of Maryland, College Park, MD, United States

1. Introduction:

Over the past 15 years, hybrid data assimilation methodologies have become more popular, particularly for use in many operational weather forecast centers worldwide. Despite its general success, hybrid DA, from a practical (and mostly operational) perspective, can become computationally expensive. Penny (2014) proposed the newest approach for the hybrid system, aiming to reduce the computational load during the composition of the final analysis. The specific algorithm proposed by Penny (2014) combines two analyses: one from the ensemble-based system and the other from the variational approach, which uses the ensemble analysis mean as the background. Thus, the final analysis is the result of this linear combination between two analyses, where the weight given to the 3D-Var is a number between 0 and 1. The goal of this work is to be used as a close to optimal weight in Penny (2014), with a dynamic weight based on the ensemble spread from the LETKF, giving more weight to the LETKF when it presents a small spread and weighing more the 3D-Var when the the LETKF presents a large spread.

2. Methodology:

We used the SPEEDY model (Simplified Parameterizations, primitiveE-Equation DYnamics), developed by Molteni (2003) in the version T30L7. The Hybrid Gain (HG) algorithm used was implemented by Wespetal (2019). It uses the LETKF from Hunt et al. (2007) and the 3D-Var from Barker et al. (2004), with a tuned background error climatology for SPEEDY computed from forecast ensemble perturbations. The HG aims to solve Equation 1 where x_{HG}^a is

the Hybrid Gain final analysis, \bar{x}_{LETKF}^a is the analysis mean from the LETKF, x_{3D-Var}^a is the analysis from the 3D-Var, which uses the ensemble analysis mean as the background, is the coefficient that determines the weight that each system will have in the final analysis ($0 \leq \alpha \leq 1$) and is a scalar.

$$x_{HG}^a = (1 - \alpha)\bar{x}_{LETKF}^a + \alpha x_{3D-Var}^a \quad (1)$$

The proposal behind the dynamical alpha is to better utilize spatially and temporally dependent information provided by LETKF through the ensemble spread. Thus, this work proposes replacing the fixed alpha (a scalar) from Equation 1 with a dynamic alpha (an evolving matrix), which is adjusted at each analysis step, each grid point in each level, and for each variable.

Eight experiments were performed using the SPEEDY model: five experiments using fixed alpha were run to estimate the best performing value of alpha (0.1, 0.3, 0.5, 0.7 and 0.9), two additional experiments using only the LETKF and only 3D-Var were performed for comparison, and the experiment using the dynamic alpha (DYN).

3. Results and conclusion:

The results were very interesting. We found good results for the dynamic alpha during the analysis (Figure 1), and better results when we look to the 120 hours forecast (Figure 2). Those results should be related to the fact that the alpha dynamic analysis, are better balanced than the others (Figures 3 and 4). This study presents a methodology that permits to identify geospatially varying values of alpha that give near-optimal results without any necessary tuning, although we highlight that the

encouraging success of this perfect model experiment does not guarantee success with all atmospheric global models.

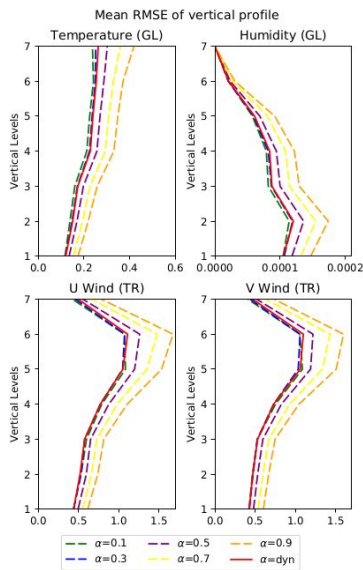


Fig 1. RMSE of vertical profile for Temperature and Humidity in the Globe, and U and V wind components in the Tropics, for the experiments with HG.

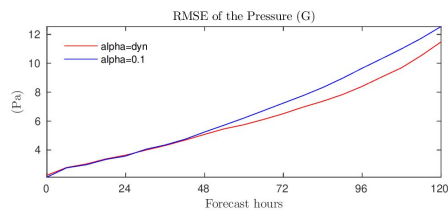


Fig 2. RMSE of the pressure during 120 hours forecast.

4. References:

Barker, D. M., W. Huang, Y.-R. Guo, A. J. Bourgeois, and Q. N. Xiao, 2004: A three-dimensional variational data assimilation system for mm5: Implementation and initial results. *Monthly Weather Review*, 132, 897–914, doi:doi:10.1175/1520-0493(2004)132<0897:ATVDAS>2.0.CO;2, URL [https://doi.org/10.1175/1520-0493\(2004\)132<0897:ATVDAS>2.0.CO;2](https://doi.org/10.1175/1520-0493(2004)132<0897:ATVDAS>2.0.CO;2)

Hunt, B. R., E. J. Kostelich, and I. SZUNYOGH, 2007: Objective weather-map analysis. *Physica D Nonlinear Phenomena*, 230 (1-2), 112–126, <http://www.sciencedirect.com/science/article/B6TVK-4MNHXX0-3/2/43ec2cf5dffe5aacdf538cdeb90cd480>.

Molteni, L., 2003: Atmospheric simulations using a gcm with simplified physical parametrizations. i: Model climatology and variability in multi-decadal experiments. *Climate Dyn.*, 20, 175–191

Penny, S. G., 2014: The hybrid local ensemble transform kalman filter. *Mon. Wea. Rev.*, 142, 2139–2149, <http://dx.doi.org/10.1175/MWR-D-13-00131.1>.

Wespelal, M. E., 2019: Advanced data assimilation for a mars atmospheric reanalysis, thesis Prospectus, University of Maryland.

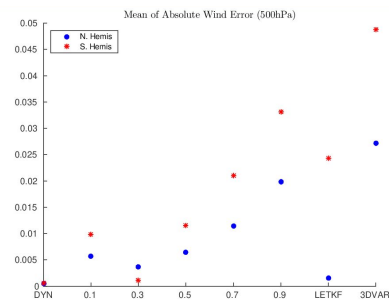


Fig 3. Mean Absolute Wind Error (500 hPa) in m/s for the 8 experiments for the (red) Southern Hemisphere and (blue) Northern Hemisphere.

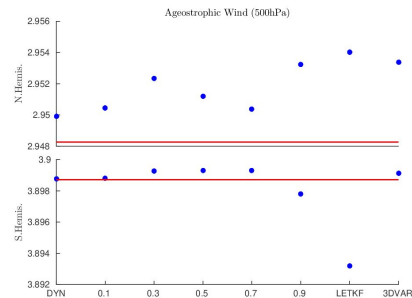


Fig 4. Mean of Ageostrophic Wind (500hPa) in m/s for the eight experiments for the Northern Hemisphere (top) and Southern Hemisphere (bottom). The blue points are the experimental values, and the red lines indicate the values for the Nature Run.

The Figures shown here come from a paper under review.

Variational Data Assimilation with Spatial and Temporal Observation Error Correlations of Doppler Radar Radial Winds

FUJITA Tadashi¹, SEKO Hiromu¹, KAWABATA Takuya¹, IKUTA Yasutaka¹,
SAWADA Ken¹, HOTTA Daisuke¹ and KUNII Masaru²

¹ Meteorological Research Institute, Japan Meteorological Agency, Tsukuba, Japan

² Numerical Prediction Division, Japan Meteorological Agency, Tokyo, Japan

e-mail: tfujita@mri-jma.go.jp

1. Introduction

High-frequency and high-resolution observations provide real-time detailed information of the atmospheric state, often related to high-impact severe weather events with small scale in time and space. In order to effectively utilize the dense observations in numerical weather prediction, it is important to appropriately handle the observation error correlation in data assimilation. This study investigates assimilation of Doppler radar radial winds, taking into account the spatial and temporal correlations of their observation errors in a variational data assimilation scheme.

2. Diagnosis of the Observation Error Correlation

The observation error correlation of Doppler radar radial winds is investigated by applying the method of Desroziers et al. (2005). The statistical samples are generated from a data assimilation cycle based on the previous version of the operational Meso-scale Analysis (MA; JMA 2019) of the Japan Meteorological Agency (JMA), replaced by the new version on 25 March 2020 (Ikuta et al. 2020). The previous MA ran a 3-hourly four-dimensional variational (4D-Var) scheme based on JNoVA (JMA Nonhydrostatic model-based Variational Data Assimilation; Honda et al. 2005), to produce the initial fields of the operational Meso-scale Model (MSM), an operational limited-area model with 5 km resolution.

The observation error correlation of Doppler radial winds from the Sapporo radar (43.14N, 141.01E) is diagnosed, based on the statistics of 1~8 Jul. 2018. During most of this period, a stationary front and a low pressure brought precipitation over this region, and Doppler radial wind data are continuously available (Fig. 1).

Figure 2 (a) displays the diagnosed correlation along the beam at the elevation angle of 1.1 deg. The half width of the correlation is about 10-20 km, increasing with distance from the radar site, consistent with Waller et al. (2016). The diagnosed temporal correlation (Fig. 2 (b)) has a half width of about 30-50 minutes, again showing an increase with the forecast time. The correlation thus looks to depend on beam propagation ranges, averaging cell volumes of radar observation (5 km x 5.625 deg.), beam widths and forecast time, suggesting contributions from representativeness and transformation errors involved with observation operator and forecast model.

3. Simple Variational Data Assimilation with Correlated Observation Error

A simple 2D-Var is used to investigate impact from incorporating correlated observation errors in data assimilation. The assimilation domain consists of 30 x 64 grid points in beam-range and azimuth-angle directions, corresponding to a resolution of 5 km x 5.625 deg. Innovations from the Sapporo radar are directory assimilated on the domain with a simple observation operator 1. The observation error correlations are approximated with Gaussian functions, with widths based on the statistics in the previous section.

Analysis increments (Fig. 3) show that including the correlation in observation errors (Fig. 3 (b)) helps to reflect detailed structures of the densely distributed innovations (Fig. 3 (a)) evenly over whole the domain, mitigating excessive increments in the case neglecting the correlation (Fig. 3 (c)) located where large innovations with identical sign are grouped (circled).

4. 4D-Var and Hybrid 4D-Var with Observation Error Correlated in Time and Space

Gaussian shaped observation error correlations are incorporated into the JNoVA 4D-Var, taking approximate spatial and temporal scales from the statistics. A hybrid 4D-Var with a flow-dependent background error is also implemented using ensemble perturbations from an EDA (Ensemble of Data Assimilations) consisting of six 4D-Var cycles with randomly perturbed observations. Doppler radar radial winds of 3 Jul. 2018 03~06 UTC from the Sapporo radar are assimilated with interval of 10 minutes using the 4D-Var and hybrid 4D-Var with assimilation windows of 3h to generate the analysis of 3 Jul. 2018 06UTC.

Figure 4 displays the time evolution of Doppler velocity increments along the beam at the azimuthal angle of 81.6 deg. (mostly east) and the elevation angle of 1.1 deg. A result from a simple variational method without temporal evolution operator is also shown for comparison. The simple variational method (b) gives increments well reflecting the innovation (a). However, the increment patterns stretch along the time axis, because the temporal evolution is not taken into account. In the 4D-Var (c), the temporal evolution operator works as an additional constraint to give increment patterns moving eastward with time, because the precipitation

area giving the Doppler velocities moves toward the east. The hybrid 4D-Var (d) reflects the eastward flow to the increment even from the early part of the assimilation window, because of the flow-dependent background error. This result suggests a high ability of the hybrid 4D-Var to extract information on the flow propagation from high-frequency observations.

Figure 5 displays RMSE against Doppler velocities from Sapporo and Kushiro (located about 280 km east of Sapporo) sites. For the hybrid 4D-Var, the results from 5 trials are shown, indicating uncertainties from the random perturbations added to the observations. The 4D-Var and hybrid 4D-Var both show main impact up to FT=6 (forecast time of 6 hours) for Sapporo (a) and up to FT=8 for Kushiro (b). The hybrid 4D-Var trials show a large diversity, but they give similar or smaller RMSEs compared to the 4D-Var for most of these periods of the experiments, suggesting a higher ability of the hybrid 4D-Var to obtain impact from the high-frequency observations. On the other hand, there are trials giving larger RMSEs than the 4D-Var for Kushiro (b) FT= -3~3, FT=9~11, and Sapporo (a) FT=6~9. This is because the times and locations not directly influenced by increments within the Sapporo observation range, which are far from the Sapporo site, might decrease the accuracy of the forecast. It is possible that there is some room for improvement in background error covariance from distant perturbations. It is one of the important

issues to investigate a sophisticated configuration of the ensemble to provide flow-dependencies for data assimilation.

Acknowledgements

This work was supported by JST AIP Grant Number JPMJCR19U2, JSPS KAKENHI Grant Number JP 19K23467, and “Advancement of Meteorological and Global Environmental Predictions Utilizing Observational ‘Big Data’ of the MEXT, Social and Scientific Priority Issues (Theme 4) to be Tackled by Using Post ‘K’ Computer” (hp180194, hp190156), Japan. This work is based on the operational NWP system developed by Numerical Prediction Division, Japan Meteorological Agency.

References

- Desroziers, G., et al., 2005: *Quart. J. Roy. Meteor. Soc.*, **131**, 3385–3396.
 Honda, Y., et al., 2005: *Quart. J. Roy. Meteor. Soc.*, **131**, 3465–3475.
 Ikuta, Y., et al., 2020: *CAS/JSC WGNE Res. Activ. Atmos. Oceanic Modell.*, **50**, 1–05.
 JMA, 2019: *Outline of the operational numerical weather prediction at the Japan Meteorological Agency. Japan Meteorological Agency*, Tokyo, Japan, 229 pp.
 Waller, J. A., et al., 2016: *Mon. Wea. Rev.*, **144**, 3533–3551.

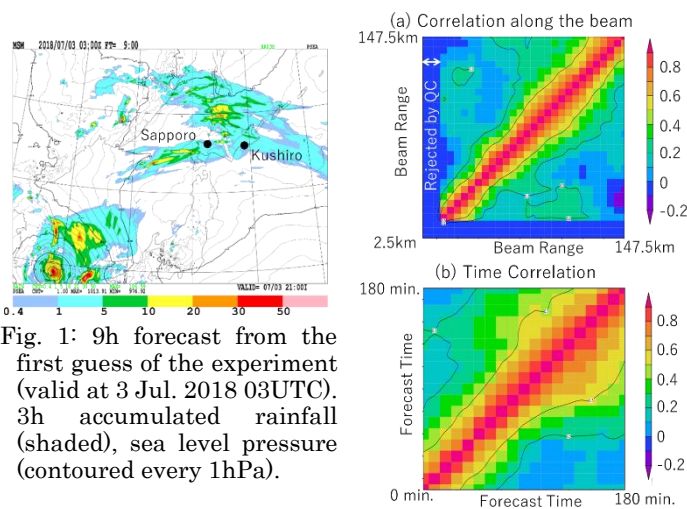


Fig. 1: 9h forecast from the first guess of the experiment (valid at 3 Jul. 2018 03UTC). 3h accumulated rainfall (shaded), sea level pressure (contoured every 1hPa).

Fig. 2: Observation error correlation of radial winds from the Sapporo Doppler radar. Statistic period is 1~8 Jul. 2018. Statistics of data at the elevation angle 1.1 deg. (a): correlation along the beam averaged over latter half of the 3h assimilation window. (b): temporal correlation averaged over beam range 47.5~97.5 km.

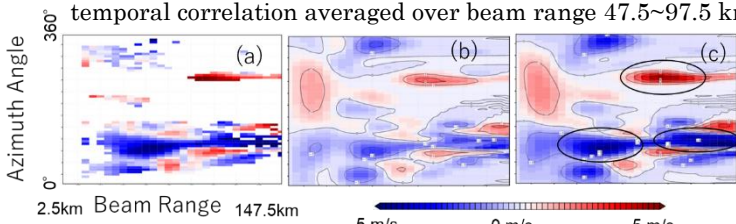


Fig. 3: Innovations and analysis increments from radial wind assimilation with the simple 2D-Var. (a) innovations, (b) increments with observation error correlations, (c) increments without observation error correlations.

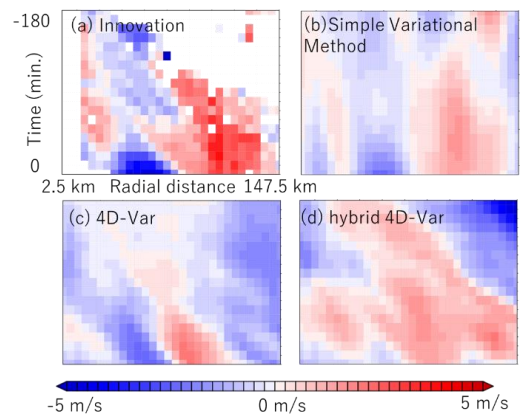


Fig. 4: Doppler velocity innovations and increments along the beam of the Sapporo radar at azimuthal angle 81.6 deg. and elevation angle 1.1 deg. Time evolution in the assimilation window (-180~0 min.).

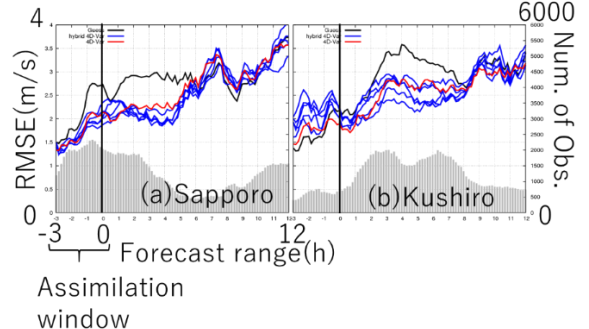


Fig. 5: RMSEs against Doppler velocity observations. (a) Sapporo radar, (b) Kushiro radar. Red: 4D-Var, Blue: 5 trials of the hybrid 4D-Var, Black: the first guess, Grey: number of observations (vertical axis on the right).

A New Data Assimilation System and Upgrading of Physical Processes in JMA's Meso-scale NWP System

IKUTA Yasutaka^{a,b*}, KUSABIRAKI Hiroshi^a, KAWANO Kohei^a, ANZAI Taro^{a,b}, SAWADA Masahiro^{a,b}, UJIIE Masashi^a, NISHIMOTO Shunsuke^a, OTA Yukinari^a and NARITA Masami^a

^aNumerical Prediction Division, Japan Meteorological Agency, Tokyo, Japan

^bMeteorological Research Institute, Japan Meteorological Agency, Tsukuba, Japan

*Correspondence to: Y. Ikuta, Meteorological Research Institute, 1-1 Nagamine, Tsukuba, Ibaraki 305-0052, Japan. E-mail: yasutaka.ikuta@mri-jma.go.jp

1 Introduction

JMA's meso-scale numerical weather prediction (NWP) system provides information for disaster mitigation based on a Meso-Scale Model (MSM) data assimilation system for forecasting. This report details an upgrade from the previous MSM1702 version (JMA 2019) to the new MSM2003 version and enhancement of related forecasting introduced at 00 UTC on 25 March 2020.

2 Data Assimilation System

Four-dimensional variational (4D-Var) data assimilation is employed to create initial MSM conditions. In the previous MSM1702 version, the forecast model was updated to the new ASUCA specifications (see Section 3.5 in JMA (2019)), while the outer/inner model in the 4D-Var data assimilation system was as per the previous system. In MSM2003, the entire data assimilation system, including the outer/inner model, was updated to allow the operation of a consistent analysis and prediction cycle system. This new ASUCA-based system is known as ASUCA-Var.

2.1 Control variables

The control variables used in ASUCA-Var are the x- and y-components of horizontal wind, underground temperature, skin temperature, surface pressure, potential temperature, soil volumetric water content and pseudo relative humidity. The underground elements here were incorporated as control variables in MSM2003 as necessary to assimilate surface and underground observations, and have significant effects on analysis results.

2.2 Tangent-linear/Adjoint model

All tangent-linear/adjoint (TL/AD) codes were recreated with the update of the dynamical and physical processes of the forecast model. The fully tangent-linearized dynamics process based on non-hydrostatics enables practically sufficient perturbation forecasting, although the TL codes of some physical processes are not implemented due to errors associated with their non-linearity.

2.3 Basic-field update

ASUCA-Var solves linear optimization problems using TL for forward integration in 4D-Var. However, the effect of the non-linear process was insufficiently incorporated in analysis values with linear optimization alone. To address this problem, a basic-field update (Trémolet 2008) was introduced to incorporate non-linear effects into optimization. The basic field is updated twice during optimization.

2.4 Variational Bias Correction

Variational bias correction (VarBC) based on the method of Cameron (2018) was implemented. In the previous assimilation system, satellite brightness temperature was pro-

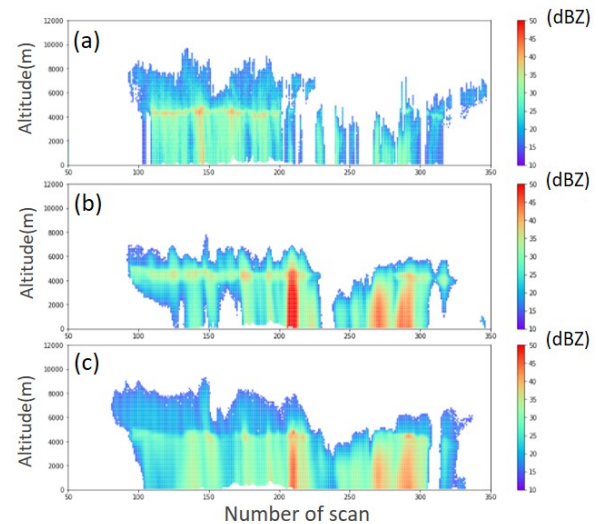


Figure 1. (a) Vertical profiles of reflectivity observed by GPM's KuPR on 7 July 2018. KuPR reflectivity simulation is based on the output of (b) MSM1702 and (c) MSM2003.

cessed with a bias correction coefficient based on the assimilation system used for JMA's global model. However, this method results in insufficient correction, and can even exacerbate the effects of the bias. VarBC solves this problem in MSM2003 and allows assimilation of bias-corrected satellite brightness temperature.

3 Forecasting System

Most of the physical processes in MSM2003 were improved, including a revision of scientific assumptions introduced into MSM1702 in addition to physical scheme enhancement. Some physical processes in MSM1702 had been tuned to improve forecast accuracy within an inconsistent system characterized by differences between the outer model and the forecast model, creating issues for performance improvement in the new system with inconsistency elimination. The updating of the physical processes in MSM2003 was designed to address this issue as outlined below.

3.1 Soil moisture

The soil moisture prediction scheme was changed from the Deardorff (1978) method to the Noilhan and Planton (1989) method to prevent significant fluctuations in soil moisture immediately after the start of forecasting and reduce errors in ground surface prediction.

3.2 Surface flux

The surface flux scheme in MSM1702 involved the use of gridded values in the middle of the layer. As the spatial discretization scheme in the MSM was applied using

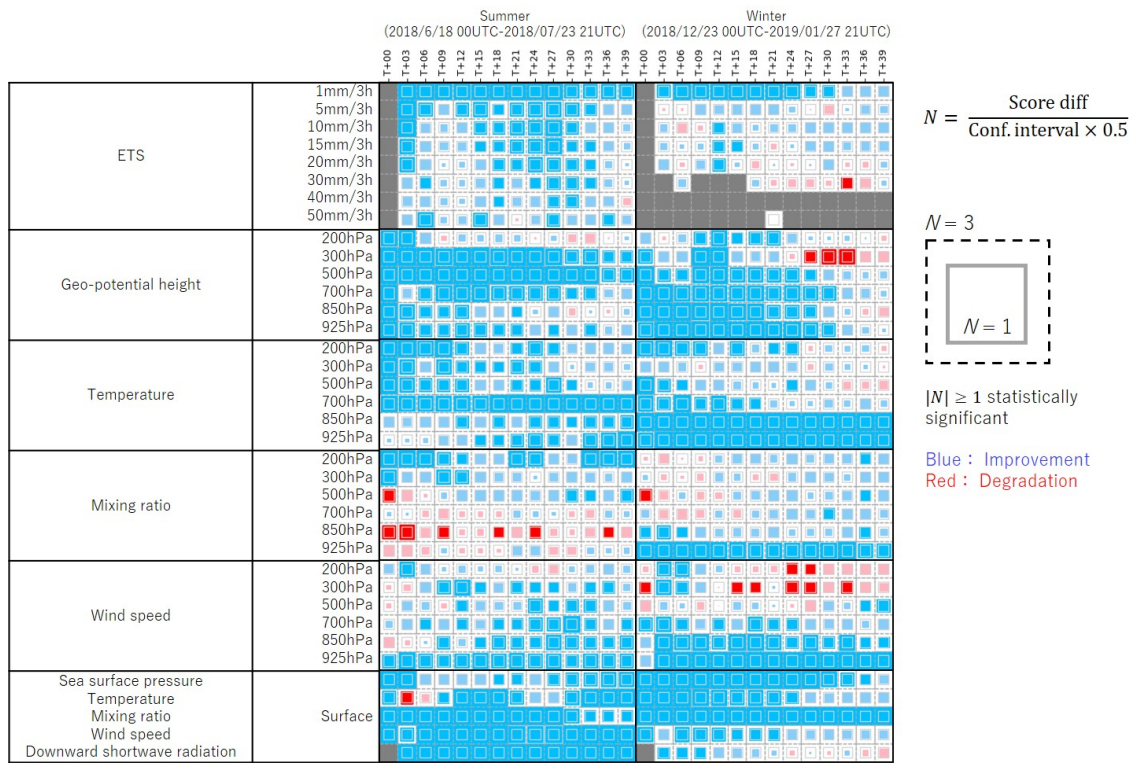


Figure 2. Observation score difference between MSM2003 and MSM1702. Columns show the score of the summer cycle from 00 UTC on 18 June 2018 to 21 UTC on 23 July 2018 and the winter cycle from 00 UTC 23 December 2018 to 21 UTC 27 January 2019, with 288 forecasts verified in each period. Square sizes indicate difference magnitude, $N > 1$ represents statistical significance, and blue/red indicate improvement and degradation, respectively.

the finite volume method, the use of gridded values as volume-averaged data should be strictly consistent. Accordingly, a new surface flux scheme based on volume averaging (Nishizawa and Kitamura 2018) was implemented in MSM2003.

3.3 Cloud

The cloud microphysics scheme was improved by revising the definition of hydrometeors and certain processes. The cloud process issues observed in MSM1702 were identified by comparing the hydrometeors of the forecast model with those from GPM satellite observation. Figure 1 shows the impact of the cloud microphysics scheme update, including improved rain profile data for the lower troposphere. Hydrometeor bias in the atmosphere was eliminated and forecast accuracy was improved.

3.4 Radiation

Upper-cloud diagnosis in the radiation scheme of MSM1702 exhibited overestimation as compared to satellite observation. The improved cloud coverage diagnosis in MSM2003 reduced errors in short-wave radiation on the ground and surface temperature.

3.5 Planetary boundary layer

Implicit treatment was adopted in the prognostic equation for mean variables based on evaluation of counter-gradient turbulent transport terms with later time-step values of turbulent variances, thereby eliminating numerical oscillation errors.

4 Impact of the upgrade

Figure 2 shows differences between MSM2003 and MSM1702 for equitable threat score (ETS) against radar/raingauge-analyzed precipitation and root mean

square error against radiosonde values over the whole domain and for surface observations in Japan. Forecast accuracy for precipitation, temperature, water vapor, geopotential height, wind speed and surface elements is significantly improved for all categories except water vapor for the lower atmosphere in summer. A slight degradation in water vapor accuracy results from a reduction of compensating errors due to excessive evaporation in the cloud microphysics scheme.

5 Summary

In this work, the new ASUCA-Var data assimilation system was introduced into operational meso-scale NWP, and the physical processes of the forecasting system were enhanced. This upgrade produced the highest improvement of forecasting quality observed in the last decade and optimized accuracy in deterministic meso-scale NWP prediction.

References

- Cameron, J. and W. Bell, 2018: The testing and implementation of variational bias correction (VarBC) in the Met Office global NWP system. Weather Science Technical Report No. 631, Met Office, 1–22.
- Deardorff, J. W., 1978: Efficient prediction of ground surface temperature and moisture, with inclusion of a layer of vegetation. *J. Geophys. Res.*, **83**, 1889–1903.
- JMA, 2019: Outline of the operational numerical weather prediction at the Japan Meteorological Agency. [Available online at <http://www.jma.go.jp/jma/jma-eng/jma-center/nwp/outline2019-nwp/index.htm>.]
- Nishizawa, S. and Kitamura, Y., 2018: A Surface Flux Scheme Based on the Monin-Obukhov Similarity for Finite Volume Models. *J. Adv. Model. Earth Syst.*, **10**, 3159–3175.
- Noilhan, J. and S. Planton, 1989: A Simple Parameterization of Land Surface Processes for Meteorological Models. *Mon. Wea. Rev.*, **117**, 536–549.
- Trémolet, Y., 2008: Computation of observation sensitivity and observation impact in incremental variational data assimilation. *Tellus*, **60A**, 964–978.

Introduction of a new hybrid data assimilation system for the JMA Global Spectral Model

KADOWAKI Takashi, OTA Yoichiro, YOKOTA Sho
 Japan Meteorological Agency, Japan
 e-mail: kadowaki@met.kishou.go.jp

1. Introduction

A four-dimensional variational (4D-Var) data assimilation system has been employed in the analysis of atmospheric conditions for the JMA Global Spectral Model (GSM) since February 2005. Evolution of initial background error covariances for the assimilation window is calculated in 4D-Var, but initial background error covariances are climatological and do not represent day-to-day weather conditions. Daily forecast uncertainties can be represented via ensemble forecasting, and various operational global numerical weather prediction centers use such forecasting data for related covariances. In this context, JMA has applied its own hybrid method composed of a Local Ensemble Transform Kalman Filter (LETKF; Hunt et al. 2007) and 4D-Var within its operational system since December 2019. This report gives an overview of the hybrid system and its impacts on forecasting.

2. Specifications of the Hybrid Data Assimilation System for the GSM

JMA (2019) outlines the Agency’s Global Ensemble Prediction System (GEPS) and the 4D-Var global data assimilation system. The LETKF used to make initial perturbations in the GEPS was imported into the 4D-Var global data assimilation system to construct the hybrid LETKF/4D-Var system. Three-hour ensemble forecasting initialized with the LETKF is used in 4D-Var with the extended control variable method of Lorenc (2003) to create flow-dependent background error covariances, which are blended with climatological background error covariances. Analysis from 4D-Var is used to re-center LETKF ensemble analysis. Figure 1 outlines the hybrid LETKF/4D-Var system, and Table 1 lists related specifications.

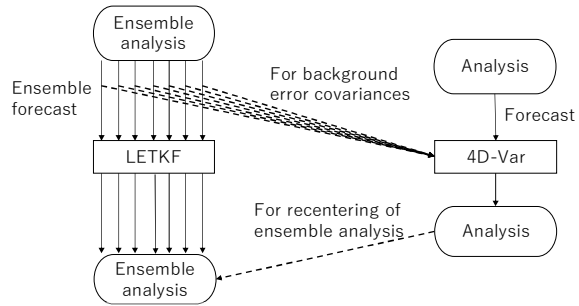


Figure 1. The hybrid LETKF/4D-Var system

Table 1. Specifications of 4D-Var in the hybrid LETKF/4D-Var system

Weighting for hybrid covariance	0.85 for climatological covariance and 0.15 for ensemble covariance under 50 hPa. They are approaching to 1 and 0 above that, respectively
Covariance inflation for ensemble covariance	Adaptive multiplicative covariance inflation (as per LETKF application). Additional covariance inflation is applied to create vertical profiles for the horizontal global mean of standard deviation from ensemble covariances consistent with those from climatological background error covariances.
Localization for ensemble covariance	Gaussian function. The localization scale for which the localization function is $1/\sqrt{e}$ is set to 800 km in the horizontal domain and 0.8 scale height in the vertical domain.
Ensemble size	50 members

3. Hybrid System Impacts on Forecasting

To verify the impacts of the hybrid LETKF/4D-Var system, a 4D-Var experiment with configuration identical to that of the operational JMA global NWP system as of October 2018 was conducted along with a hybrid LETKF/4D-Var experiment. Both covered the period from June 2 to October 11 2018, which included forecasting for tropical cyclones (TCs) from T1804 to T1825 in the western North Pacific.

Ensemble forecasting initialized with the LETKF showed the capacity for background error covariance creation dependent on day-to-day weather conditions as exemplified in Figure 2 (a) (extratropical cyclone, tropical cyclone and tropical depression) and 2 (b) (indicating a larger ensemble

spread around these phenomena than in other areas). Figure 2 (c) shows average TC position errors for the western North Pacific from both experiments. The results from the hybrid LETKF/4D-Var experiment are slightly better. Figure 3 shows the zonal mean of the improvement ratio for geopotential height forecasting from the hybrid LETKF/4D-Var experiment relative to that of the 4D-Var experiment. Improvements in geopotential height forecasting for the mid-latitudes in particular were observed in the winter hemisphere and elsewhere, as well as in the boreal winter experiment (not shown). The new system has been operated by JMA since December 2019.

References

- Hunt, B. R., E. J. Kostelich, and I. Szunyogh, 2007: Efficient data assimilation for spatiotemporal chaos: a local ensemble transform Kalman filter. *Physica. D.*, **230**, 112 – 126.
- JMA, 2019: Outline of the operational numerical weather prediction at the Japan Meteorological Agency, Appendix to WMO Technical Progress Report on the Global Data-processing and Forecasting System (GDPFS) and Numerical Weather Prediction (NWP) Research. Japan Meteorological Agency, Tokyo, Japan.
- Lorenc, A. C., 2003. The potential of the ensemble Kalman filter for NWP: a comparison with 4D-Var. *Quart. J. Roy. Meteor. Soc.*, **129**, 3183 – 3203.

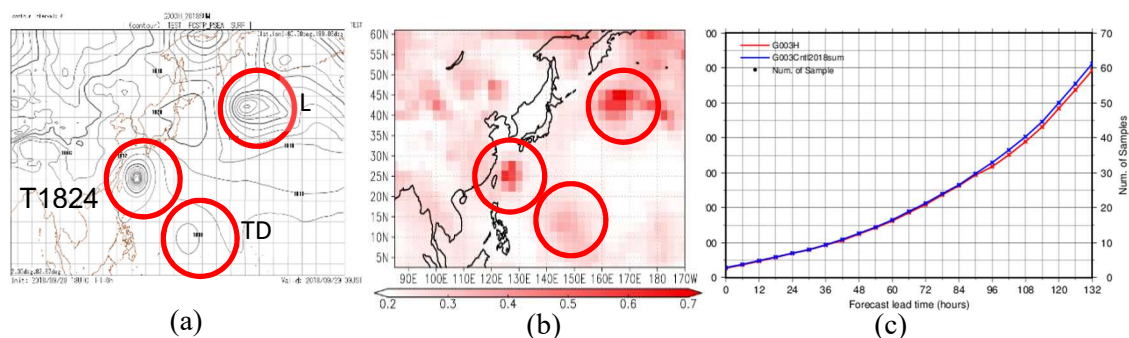


Figure 2. Six-hour forecasting for (a) sea-level pressure and (b) sea-level pressure spread, both from the hybrid LETKF/4D-Var experiment with initialization at 1800 UTC on 28 Sep 2018. (c) Average TC position errors for TCs from T1804 to T1825 in the western North Pacific. Blue: 4D-Var experiment; red: hybrid LETKF/4D-Var experiment

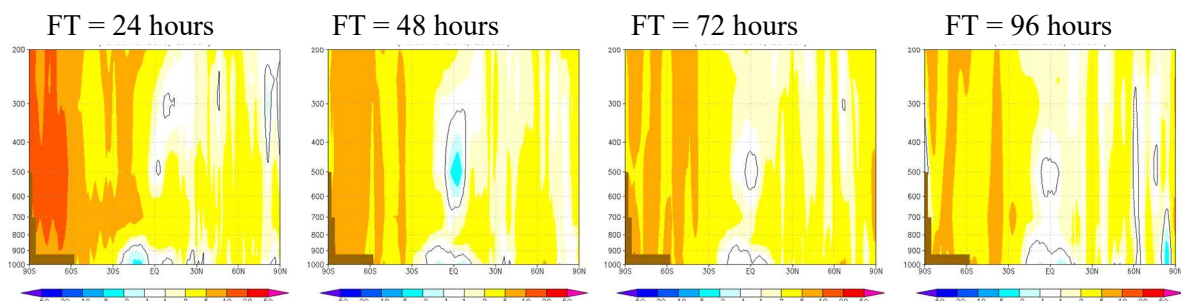


Figure 3. Zonal mean of relative improvement ratio [%] for the hybrid LETKF/4D-Var experiment against that of the 4D-Var experiment in terms of RMS error against ECMWF analysis for geopotential height forecasting. Warm colors indicate forecast error reduction. The validation period is from 1st July to 30th September 2018 (92 days).

A Traceable Observing System Experiment in NCEP GODAS

Hyun-Chul Lee*, David Behringer* and Daryl Kleist**
(*IMSG @ NOAA/NWS/NCEP/EMC, **NOAA/NWS/NCEP/EMC)
email : hyun-chul.lee@noaa.gov

The National Centers for Environmental Prediction (NCEP) currently operates two versions of the Global Ocean Data Assimilation System (GODAS, Behringer, 2007). The first of these runs is in a stand-alone format forced by the surface fluxes from the NCEP Climate Data Assimilation System (CDAS2) atmospheric reanalysis. It runs in near real-time on a daily basis and serves as a tool for monitoring the evolution of the global ocean state. The second version runs as part of the NCEP operational Climate Forecast System (CFSv2) based on the Modular Ocean Model (MOM4) at a resolution of one half degree, and provides the initial states for the ocean component of CFSv2. Analysis products from GODAS are fundamental to NCEP's operational efforts for not only monitoring the ocean state but also for forecasting multi-week to seasonal variability in the NCEP CFS.

NCEP GODAS assimilates remotely sensed sea surface temperatures, and in situ profiles of temperature and salinity from EXpendable BathyThermograph (XBT) and Conductivity Temperature Depth (CTD), stationary fixed moorings, and autonomous Argo floats. These ocean observing systems play a critical role in the quality of GODAS products. In order to evaluate the

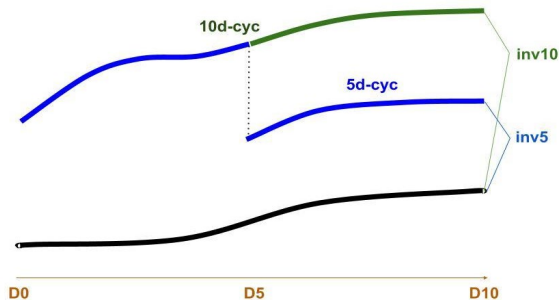


Figure 1. Two trajectories of 10day (green) and 5day (blue) cycle runs, and real Observations (black) in time. 10day and 5day cycle runs start at the same time, and the restart of 5day cycle run from Analysis field (dashed line).

impact of the observing system on NCEP operational products, a series of observing system experiments have been carried out, and the observational innovations and the analysis increments associated with individual ocean observations in NCEP's GODAS are evaluated.

In the traceable observing system experiments (tOSE), the impacts of the observing systems on the GODAS are defined from the squared differences of observation innovations between 5 day and 10 day cycle runs. Fig. 1 shows a schematic diagram of the tOSE for 5 day/10 day cycle runs. At the end of the two

runs, the differences are due to the updated initial states of the 5 day run. From the results of these differences, it is possible to estimate the impacts of each observing system on the GODAS, which is traceable at each observation in space and time.

Fig. 2 shows the seasonal trajectories of analysis increments along the Argo floats. As shown in Fig. 2, the increments from Argo floats are generally positive in the central and eastern tropical Pacific in spring and summer of 2015, which corrects the cold bias in GODAS. Overall, the increments in the spring-summer seasons are larger than that in the fall-winter seasons, and it is

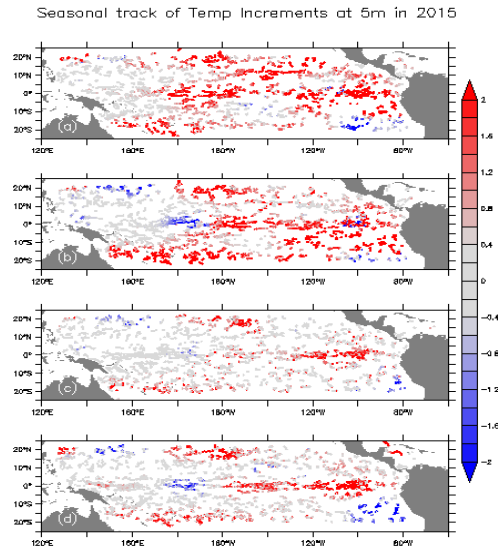


Figure 2. Seasonal trajectories of analysis increments of temperature at 5 m depth along the Argo floats in JFM (a), AMJ (b), JAS (c) and OND (d) from the 5 day cycle run (°K).

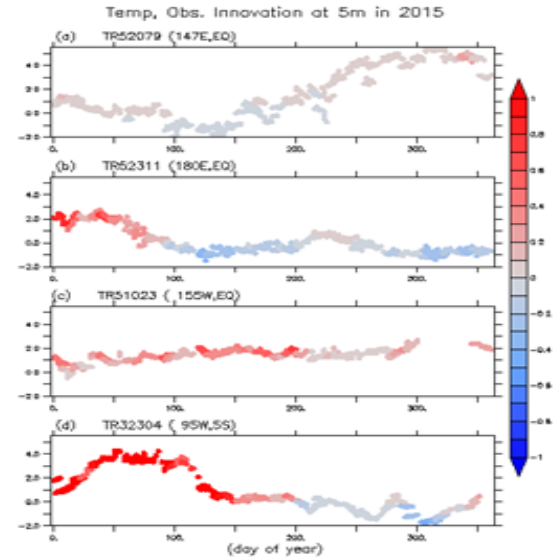


Figure 3. Time variations of observational increments of temperature at 5 m depth innovation of 5m depth temperature from mooring buoys at (147E, EQ) (a), (180E, EQ) (b), (155W, EQ) (c), (95W, 5S) (d). Analysis

suggested that the impacts of Argo floats are stronger in northern winter and spring than during the other half of this year in the tropical Pacific. At 50 m depth (not shown here), the impacts of Argo mainly take place along the seasonal thermocline.

Fig. 3a shows that in the western warm pool region, there occurs a relatively large model – observation differences for moored buoys in late autumn and early winter. While the signs of the increments are consistent with the differences there is not a simple linear relationship between their magnitudes. In Fig. 3b, differences in the mooring buoys are relatively large in winter and early spring 2015, and it suggests that the mooring buoy is having a strong impact on the model analysis in this season. There is clearly useful information on the impacts of mooring buoys, but care should be taken in interpreting that information. The question as to whether it indicates a fault with the mooring or a persistent bias in the GODAS analysis could be resolved by considering the differences at adjacent moorings or at Argo floats which are nearby in space and time.

Acknowledgements: This study was supported by NOAA’s Global Ocean Monitoring and Observing Program.

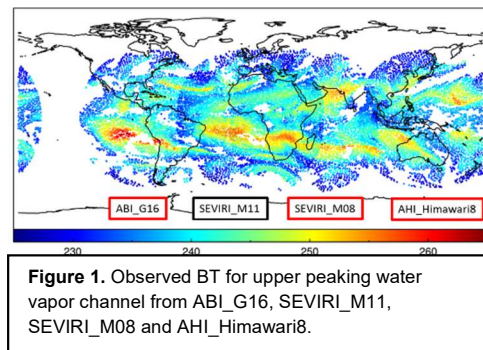
Reference: Behringer, D. W., 2007: The Global Ocean Data Assimilation System (GODAS) at NCEP. Proc. 11th Symp. Integr. Obs. Assim. Systems, San Antonio, TX, Amer. Meteor. Soc. 3.3.

Clear-Sky Radiance (CSR) Assimilation from Geostationary Infrared Imagers at NCEP

Haixia Liu^{1,2}, Andrew Collard^{1,2}, James Jung³ and Daryl Kleist²
1. *IMSG, Rockville, MD, U.S.A.* 2. *NCEP/EMC, College Park, MD, U.S.A.*
3. *CIMSS, University of Wisconsin*
Email: Haixia.Liu@noaa.gov

1. CSR Products from Geostationary Infrared Imagers

Clear-Sky Radiance (CSR) is a product that has been generated by averaging brightness temperatures (BTs) from the clear pixels identified by a cloud mask within a processing segment. Only the CSR from the Spinning Enhanced Visible and Infrared Imager (SEVIRI) on Meteosat-11 (M11) is currently assimilated in operations at the National Centers for Environmental Prediction (NCEP). Several additional CSR products have recently become available in BUFR format, including the Advanced Baseline Imager (ABI) on GOES-16 (G16), the Advanced Himawari Imager (AHI) and the SEVIRI on Meteosat-08 (M08). These CSR products are similar with a few minor differences, such as ABI CSR having higher temporal resolution and its clear-pixel percentage within a processing segment not being channel dependent. Investigations have been performed on the impact of these additional CSR products on global analysis and forecast skill using NCEP's Finite-Volume on a Cubed-Sphere Global Forecast System (FV3GFS) system. This work will be briefly discussed in this paper and will be included in the next implementation of the FV3GFS. Figure 1 shows the global coverage of all four CSR products. The CSR data in the figure are already thinned to 145km.



2. Evaluations of CSR products

The geostationary CSR data assimilation focuses on the water vapor (WV) channels only. The weighting functions of these WV channels from all four instruments are plotted in Fig.2. All four instruments have similar weighting functions for the upper-level WV channel. Only ABI and AHI have the mid-level channel and show similar features. ABI and AHI are more similar to each other than to SEVIRI for the lower-level channel. The SEVIRI instruments are more sensitive to the lower troposphere.

The CSR data quality for each instrument has been evaluated through studying the statistical characteristics of the CSR products compared with their simulated model equivalences using the operational FV3GFS model forecast and Community Radiative Transfer Model (CRTM) as the forward operator, so-called first guess (FG) departures. Figure 3 shows normalized FG departure histograms for all of the four instruments on the same plot for easy comparison. The three panels (a), (b), and (c), respectively, represent the upper-, mid- and lower-level WV channels. The data samples span the whole month of May 2019 over both sea and land surfaces after quality control has been applied. Solid lines represent the FG departures before bias correction is conducted. It is clear that these instruments have different biases, but their FG departures all have a Gaussian distribution of very similar shape, except for the lower-level WV channel. The standard deviations are larger for SEVIRI, especially for SEVIRI_M08, possibly because the SEVIRI lower-level WV channels are more sensitive to the lower part of the atmosphere according to the weighting function plot in Fig. 2. In addition, the SEVIRI_M08 covers more of the land than the SEVIRI_M11 shown in Fig. 1. The FG departures after bias correction are shown in dashed lines in these plots where all the biases become nearly zero. For the lower-level channel, SEVIRI_M08 (in magenta)

has a lower peak. The variational bias correction performs reasonably well in correcting the biases for these four different instruments.

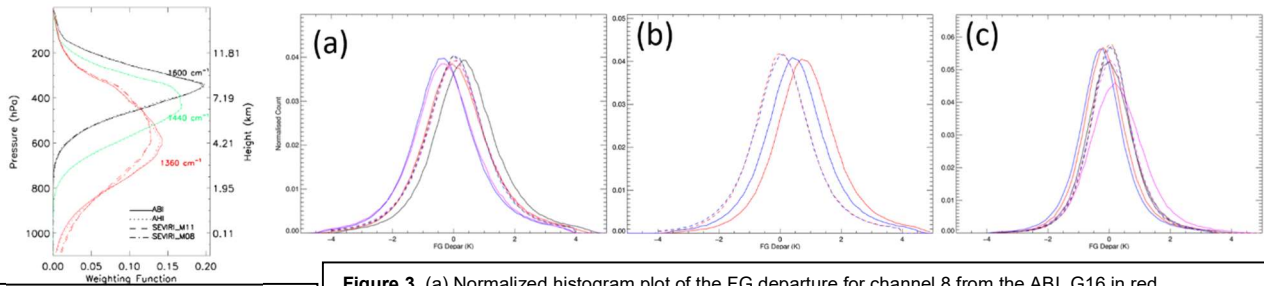


Figure 2. Weighting functions of the WV channels from the instruments ABI_G16, AHI, SEVIRI_M11 and SEVIRI_M08.

Figure 3. (a) Normalized histogram plot of the FG departure for channel 8 from the ABI_G16 in red, AHI_Himawari8 in blue, and channel 5 from the SEVIRI_M08 in magenta and SEVIRI_M11 in black. The solid and dashed curves are before and after the bias correction. (b) the same for channel 9 from ABI_G16 and AHI_Himawari8. (c) the same for channel 10 from ABI_G16 and AHI_Himawari8 and channel 5 from the SEVIRI_M08 and SEVIRI_M11.

3. Assimilation Experiment Configuration and Results

A set of parallel experiments were performed utilizing the Gridpoint Statistical Interpolation's hybrid 4D-EnVar in NCEP's Global FV3GFS Data Assimilation System (GDAS), with the operational configuration at a reduced resolution of C384 for the deterministic component and at the C192 for the 80 ensemble members, covering the period of April 23 to June 30, 2019. The first week of the experiments was used to spin up the bias correction coefficients which are initialized from zero. The months of May and June were used for verification to evaluate the additional CSR data impact on the global analysis and forecast skill. The CSR data from the WV channels on the ABI_G16, AHI_H08 and SEVIRI_M08 were assimilated in the experiment while they were passively monitored in the control run. The assigned observation errors were estimated from the globally averaged Observation minus Forecast statistics. Figure 4(a) shows the relative humidity (RH) analysis increment root-mean-square (RMS) error is reduced by assimilating additional CSR data, which implies improvement in the first guess relative humidity fields. This is consistent with more Microwave Humidity Sensor (MHS) data on Metop-A being assimilated for most of the cycles, as shown in Fig. 4(b).

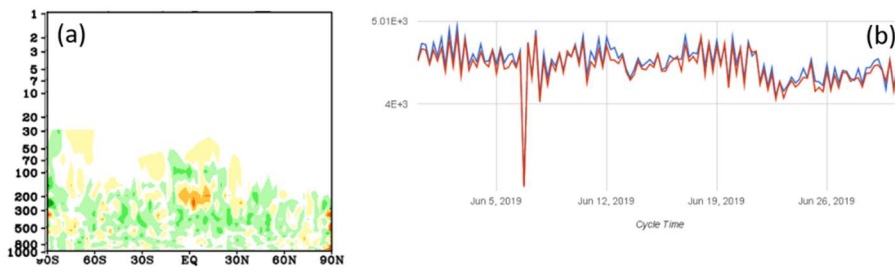


Figure 4. (a) Differences of the RH analysis increment RMS error between the experiment and the control. Green color represents RMS is reduced in the experiment. (b) Time series plot of the assimilated MHS-Metop-A data counts. Blue line is the experiment with additional CSRs assimilated and red is the control.

Acknowledgments

Thanks to Steve Stegall, Sudhir Nadiga and Kate Friedman at NCEP/EMC and Qiang Zhao, Peter Keehn and Tom King at NESDIS for supporting the geostationary CSR real-time BUFR data. Thanks to Yong Chen for providing the weighting function plot. Fanglin Yang and Mary Hart are thanked for proofreading the draft.

Preliminary results of soil moisture data assimilation into JMA Global Analysis

Kenta Ochi

Climate Prediction Division, Japan Meteorological Agency, Tokyo, Japan
(E-mail: k_ochi@met.kishou.go.jp)

1. Introduction

The Japan Meteorological Agency (JMA) uses climatological monthly mean soil moisture data to provide initial conditions for the land model of its Global Spectral Model (GSM). However, this configuration could potentially degrade forecast results, especially for the lower atmosphere, because the data do not represent day-to-day variations in initial soil moisture. To improve the quality of such moisture and lower-atmosphere conditions, a simplified Extended Kalman Filter (SEKF; Drusch et al., 2009, de Rosnay et al., 2013) has been tested with JMA Global Analysis (GA). A numerical weather prediction (NWP)-type experiment and related evaluation against in-situ observation have also been executed to assess the impacts of the soil moisture analysis cycle.

2. Assimilation method

In the SEKF, the analyzed state vector \mathbf{x}_a is computed at time t_i for each grid point as

$$\mathbf{x}_a(t_i) = \mathbf{x}_b(t_i) + \mathbf{K}_i[\mathbf{y}_o(t_i) - H_i(\mathbf{x}_b)]$$

where \mathbf{x}_b is a first-guess state vector, \mathbf{y}_o is an observation state vector and H_i is a nonlinear observation operator. The Kalman gain matrix \mathbf{K}_i is computed as

$$\mathbf{K}_i = [\mathbf{B}^{-1} + \mathbf{H}_i^T \mathbf{R}^{-1} \mathbf{H}_i]^{-1} \mathbf{H}_i^T \mathbf{R}^{-1}$$

where \mathbf{B} is a background-error covariance matrix and \mathbf{R} is an observation-error covariance matrix. Following de Rosnay et al. (2013), these are static and diagonal matrices composed of error variances. \mathbf{H}_i is a linearized observation operator approximated from finite differences using individual perturbations of the model state vector.

Analysis-based screen-level parameters and an ASCAT surface soil moisture product (Bartalis et al., 2007) are assimilated in the SEKF. The former are calculated via optimal interpolation using 2-m temperature (T_{2m}) and relative humidity (RH_{2m}) data as reported in SYNOP observations, while the latter is matched to the soil moisture climatology of the JMA land model using cumulative distribution function (CDF) matching before SEKF application.

3. Experimental settings

Figure 1 shows the specifications of the NWP-type experiments, all of which were based on the operational GA and GSM as of Nov. 2019 except for the SEKF used in the TEST experiment. In the JMA land model, soil is discretized into seven layers with thicknesses of $\Delta z = 0.02, 0.05, 0.12, 0.3, 0.5, 1.0$ and 1.5-m. To prevent unrealistic soil moisture drift during long-term integration, initial soil moisture between the fourth and seventh layers was set as climatological values in the TEST experiment. Such configuration can be rationally applied to deeper layers in consideration of low sensitivity among the Jacobians of T_{2m} and RH_{2m} .

4. Verification results

Figure 1 shows that initial conditions of soil moisture determined from the SEKF cycle (TEST experiment) can be used to represent day-to-day variations. SEKF introduction improved the RMSEs of temperature at 850 hPa verified against ECMWF and UKMO analysis for land areas (e.g., Central Asia, Australia, North America and South America; Figure 2). Figure 3 shows normalized changes in the standard deviation of the first-guess departure for radiosonde observations on temperature and relative humidity. SEKF application improved statistics in the lower atmosphere, especially in the Northern Hemisphere. Forecast skill for lower temperature and humidity in the short range were also improved by 4% in the Northern Hemisphere (Figure 4).

5. Summary and future works

The quality of lower-atmosphere initial conditions was improved by introducing the SEKF to the JMA GA. The improved initial soil moisture and lower-atmosphere conditions produced better forecast skill for the near-surface atmosphere. Based on these results, the SEKF is planned to be introduced as part of near-future GA upgrades.

As no clear improvement is currently seen on sub-seasonal to seasonal timescales, future focus needs to be placed on enhancement with extended-range forecasts.

Table 1: Specifications of each NWP-type experiment.

	CNTL (operational version)	TEST
Forecast model	<input type="checkbox"/> GSM 1705 (JMA, 2019) <input type="checkbox"/> TL959L100 (approx. 20km, 100 vertical levels up to 0.01hPa)	
Initial conditions of atmosphere	<input type="checkbox"/> 4D-Var global objective analysis	
Initial conditions of land model	<input type="checkbox"/> Soil moisture content: climatological values using offline model forced by GSWP3(Kim, 2017) <input type="checkbox"/> Snow water equivalent: Snow analysis (2D-OI) <input type="checkbox"/> Other variables: forecast guess	<input type="checkbox"/> Soil moisture content: Soil analysis (SEKF) <input type="checkbox"/> Observations: SYNOP (T_{2m} , RH_{2m}), Metop-A,B (ASCAT soil moisture)
Period	<input type="checkbox"/> Jun. 10, 2017 to Oct. 11, 2017	

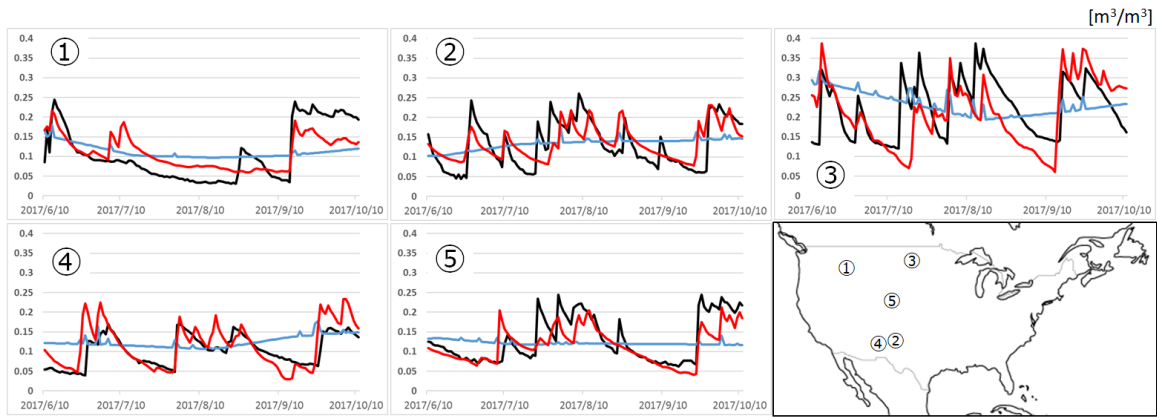


Figure 1: Comparison of soil moisture analysis in the second layer with USDA SCAN observations (at a depth of 5 cm) for five sites from July to September 2017. Black: USDA SCAN; blue: CNTL; red: TEST.

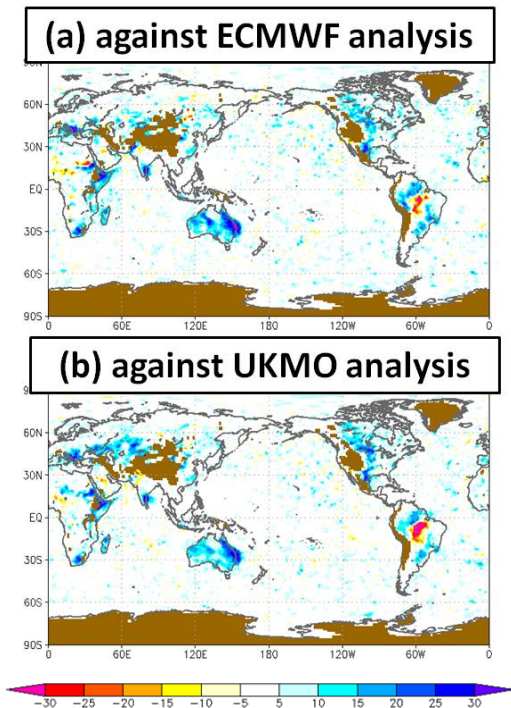


Figure 2: Percentage of relative improvement in root mean square error for 24-hour forecasts of temperature at 850 hPa verified against (a) ECMWF and (b) UKMO operational analysis.

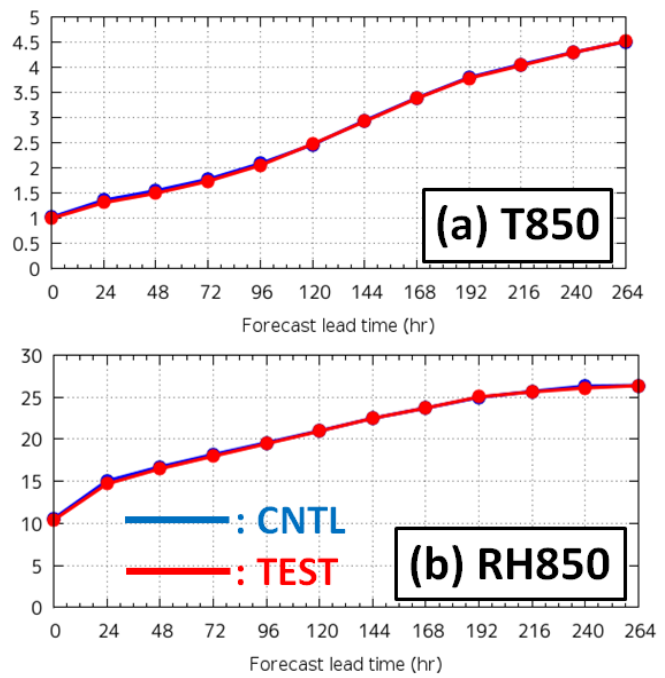


Figure 4: Root mean square error of (a) temperature at 850 hPa (b) relative humidity at 850 hPa against radiosondes in the Northern Hemisphere (20 – 90°N) for July to September 2017.

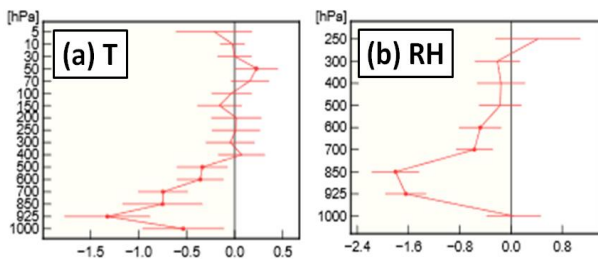


Figure 3: Normalized changes in the standard deviation of first-guess departures for radiosondes in the Northern Hemisphere (20 – 90°N): (a) temperature (b) relative humidity. Error bars: 95% confidence intervals.

References

- Bartalis, Z., Wagner, W., Naeimi, V., Hasenauer, S., Scipal, K., Bonekamp, H., Figa, J., and Anderson, C, 2007: Initial soil moisture retrievals from the METOP-A Advanced Scatterometer (ASCAT). *Geophys. Res. Lett.*, **34**, L20401, doi:10.1029/2007GL031088.
- Drusch, M., Scipal, K., de Rosnay, P., Balsamo, G., Andersson, E., Bougeault, P., and Viterbo, P., 2009: Towards a Kalman Filter based soil moisture analysis system for the operational ECMWF Integrated Forecast System. *Geophys. Res. Lett.*, **36**, L10401, doi: 10.1029/2009GL037716.
- Japan Meteorological Agency, 2019: Outline of Operational Numerical Weather Prediction at JMA. Japan Meteorological Agency, Tokyo, Japan.
- Hyungjun Kim., 2017: Global Soil Wetness Project Phase 3 Atmospheric Boundary Conditions (Experiment 1) [Data set]. Data Integration and Analysis System (DIAS). <https://doi.org/10.20783/DIAS.501>.
- de Rosnay, P., M. Drusch, D. Vasiljevic, G. Balsamo, C. Albergel, and L. Isaksen, 2013: A simplified extended Kalman filter for the global operational soil moisture analysis at ECMWF. *Quart. J. Roy. Meteor. Soc.*, **139**, 1199–1213.

Operational use of GOES-16 clear-sky radiance (CSR) data in JMA's global NWP system

OKABE Izumi

Numerical Prediction Division, Forecast Department, Japan Meteorological Agency

E-mail: i-okabe@met.kishou.go.jp

1. Introduction

Clear-sky radiance (CSR) data from five operational geostationary satellites (Himawari-8, two Meteosat Second-Generation (MSG) and two GOES) are utilized in JMA's global numerical weather prediction (NWP) system. With the retirement of GOES-13 (the predecessor to GOES-East, operating at a longitude of 75 degrees west) on January 8 2018, data acquisition of GOES-16 CSR was started on April 16 2018, leaving a four-month observation void in JMA. Data quality evaluation based on first-guess (FG) departure (i.e., the difference between observed and simulated brightness temperatures) statistics and assimilation experiments conducted by JMA verified the benefits of using GOES-16 CSR data, which were incorporated into the Agency's operational global NWP system on June 4 2019. This report gives an overview of GOES-16 CSR data evaluation within the JMA system.

2. GOES-16 CSR data evaluation

The 16 bands of the GOES-16 Advanced Baseline Imager (ABI) include three water-vapor (WV) bands (8, 9 and 10) with central wavelengths of 6.2, 6.9 and 7.3 micrometers, respectively. As ABI is a similar instrument to the Advanced Himawari Imager (AHI), whose CSR data are currently assimilated in JMA's NWP systems, the quality control (QC) method used for Himawari-8 was applied to GOES-16 CSR data. Since these data are produced assuming under clear-sky conditions, cloud-affected data need to be removed before assimilation. Thus, CSR data with a low clear-pixel ratio and a large standard deviation (STD) of brightness temperature in a particular segment (consisting of 32 x 32 pixels for CSR data production) are eliminated. To remove cloud-affected data, WV-band CSR data with clear-pixel ratios under 90% or STD values larger than 1 K are rejected in QC. With clear-pixel ratios for the window band (band 13) below the relevant thresholds (55, 60 and 65% for bands 8, 9 and 10, respectively), WV CSR data in the same segment are rejected.

The radiative transfer (RT) calculation developed for Himawari-8 and MSG CSR data

(Okabe 2019) is applied to GOES-16 CSR data. This approach involves the use of retrieved land surface temperature rather than FG skin temperature to improve the accuracy of simulated brightness temperature, especially for surface-sensitive bands.

To evaluate the quality of GOES-16 CSR data, FG departure statistics in QC-processed data were compared to those of Himawari-8 CSR data. Passively monitored (i.e., without assimilation) GOES-16 CSR data were used for the FG departure statistics, and data from Himawari-8, two MSGs and GOES-15 CSR data including other observations were actively assimilated. Two geostationary satellites were used for CSR observation in the GOES-16 area (Meteosat-11 for the eastern part, GOES-15 for the western part). Figure 1 shows horizontal distributions of root mean squares (RMSs) of FG departures for the two satellites. The RMS of GOES-16 in the area outside overlapping with other geostationary satellites was larger than those of Himawari-8, suggesting that background quality was degraded in the CSR gap area after the retirement of GOES-13. Meanwhile, RMSs in overlapping areas were as small as those of Himawari-8, and the quality of QC-processed GOES-16 CSR data was assumed to be similar to that of Himawari-8.

3. Assimilation experiments

Assimilation experiments were conducted to determine the impact of GOES-16 CSR data on global analysis and forecasting. The control experiment (referred as CNTL) had the same configuration as the operational JMA global NWP system as of December 2018, and the test experiment (referred as TEST) was the same as CNTL except for the assimilation of three WV bands of CSR data from GOES-16. The experiments covered the periods from June 10 to October 11 2018 and from November 10 2018 to March 11 2019.

4. Impacts on analysis and forecasting

Figure 2 shows normalized changes in STD values for the FG departure between TEST and CNTL for brightness temperatures from the microwave humidity sounder (MHS) and the Advanced Microwave Sounding Unit-A (AMSU-

A), and relative humidity from radiosonde observation. Reduced STD values indicate improved FG fields, especially for water vapor. The values here are generally reduced, indicating significant MHS improvement. Figure 3 shows horizontal distributions of differences in the STD of FG departure for MHS data between TEST and CNTL, with reduced STD values observed in the GOES-16 CSR coverage area. As MHS is sensitive to WV in the middle-to-upper troposphere, this result suggests a positive impact on WV field accuracy for the FG from GOES-16 CSR assimilation. Figure 4 shows the vertical zonal mean of forecast field relative improvement for specific humidity and geopotential height (defined as the difference between the CNTL and TEST root mean square error (RMSE) divided by the RMSE of CNTL). The improvements in analysis (0-day forecasts) were retained for up to two-day forecasts for the humidity and geopotential height fields at low and mid-latitudes in the troposphere.

5. Summary

On June 4 2018, JMA began assimilating GOES-16 CSR data based on the QC method developed for Himawari-8. Evaluation showed that RMSs of FG departure for GOES-16 CSR were as small as those for Himawari-8 CSR in areas of overlap with other geostationary satellites, and the quality of GOES-16 CSR data was deemed to be similar to that of Himawari-8 data. Experiments showed a positive impact from GOES-16 CSR data assimilation on the WV field accuracy of FG in the mid-to-upper troposphere, especially in the central part of the GOES-16 observation area. The forecast fields of humidity and geopotential height were improved in forecasts of up to two days in the low- and mid-latitudes of the troposphere.

References

Okabe, I. (2019). Operational use of surface-sensitive clear-sky radiance data in JMA's global NWP system. *CAS/JSC WGNE Research Activities in Atmospheric and Oceanic Modeling, Rep.*, **49**, 1-15.

Acknowledgements

C3S Copernicus Climate Change Service (2017). ERA5: Fifth Generation of ECMWF Atmospheric Reanalysis of the Global Climate. Copernicus Climate Change Service Climate Data Store (CDS). Accessed on 10 June 2019, <https://cds.climate.copernicus.eu/cdsapp#!/home>

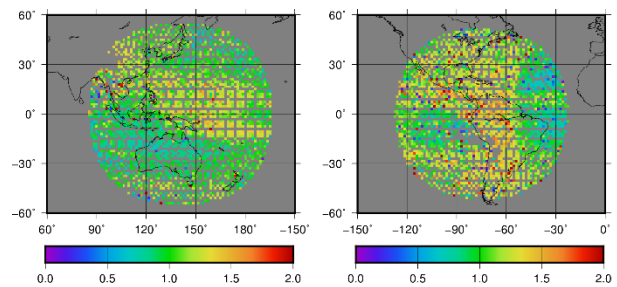


Figure 1. Root mean square of first-guess departures for Himawari-8 (assimilated, left) and GOES-16 (not assimilated, right) for August 2018 based on post-QC CSR data

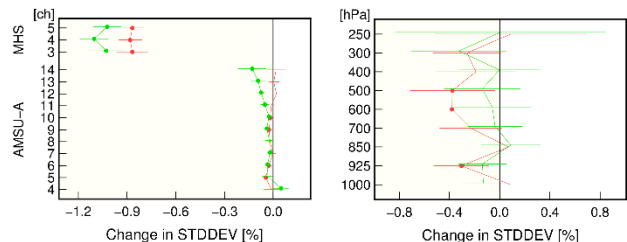


Figure 2. Normalized changes in standard deviation (STDDEV) for first-guess departures in microwave sounding data for individual channels [ch] (left) and radiosonde observation data indicating relative humidity for individual pressure heights [hPa] (right). The validation periods are from June 21 to October 11 2018 (red dots) and from November 21 2018 to March 11 2019 (green dots).

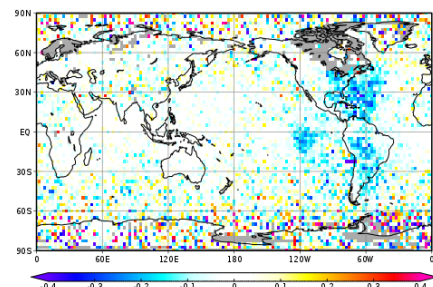


Figure 3. Normalized changes in the standard deviation of first-guess departures for MHS (channel 3) [%]. The validation period is from June 21 to October 11 2018.

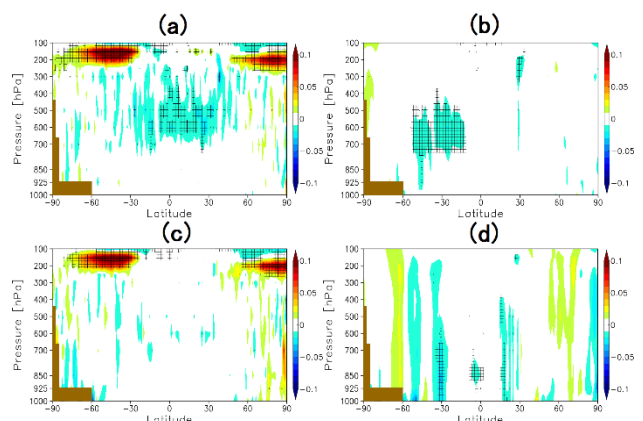


Figure 4. Zonal mean of relative improvement in root mean square errors for 0-day (top) and 2-day (bottom) forecasts for (a), (c) specific humidity and (b), (d) geopotential height based on calculation using forecasts from 12 UTC initials and ERA5 analysis for verification. The verification period is from July 1 to September 30 2018.

Impact of Data Assimilation of Shipborne GNSS Data on Rainfall Forecast (Part 2)

Seko Hiromu and Shoji Yoshinori

Meteorological Research Institute / Japan Meteorological Agency

e-mail: hseko@mri-jma.go.jp

1. Introduction

Heavy rainfalls occur almost every year in Japan. Airflows that supply water vapor to heavy rainfalls originate from the Oceans around Japan. The accurate observation of water vapor over the Oceans is essential to increase the accuracy of rainfall forecast (fig. 1). In this study, precipitable water vapor (PWV, water vapor amount in column) observed by GNSS on vessels (shipborne GNSS) was assimilated using the Meso-NAPEX (Numerical Analysis and Prediction EXperiment system), which was implemented to the data assimilation system of the Meteorological Research Institute. A few cases in which data assimilation of shipborne GNSS data improved the rainfall forecasts were reported (Seko et al. 2019). In this report, the impacts caused by bias correction of shipborne GNSS PWV and by the number of observations are explained.

2. Shipborne GNSS data

The GNSS data that was observed by eight vessels (freighters) on the western side of Kyushu island were used in this study. GNSS PWV was retrieved using the procedure tried by Shoji et al. (2017). This area is located on the upstream side of the low-level inflow that supply water vapor to the rainfall systems over the Kyushu. The bias and standard deviation between the shipborne GNSS PWV and the mesoscale analysis (MA, 3 hourly and 5 km resolution) of Japan Meteorological Agency (JMA) are -0.56 mm and 2.56 mm, respectively (Shoji et al, 2019).

3. Specification of data assimilation method

The Meso-NAPEX is a quasi-operational data assimilation system which enables us to make data assimilation experiments. The horizontal resolution of the Meso-NAPEX is 5 km. The data assimilation window is 6 hours and the observation data are assimilated every hour. As the target event for this report, the rainfall system that passed through the northern Kyushu on 27-28th Aug. 2019 was adopted. This rainfall system caused the flooding and landslides there and killed 4 people.

We performed 7 experiments (table 1). In **CNTL**, the conventional data of JMA including the satellite data were assimilated by using the Meso-NAPEX. The PWV data of shipborne GNSS (SGP) were added to the conventional data in **SN**. Because of the bias between MA and SGP, the bias corrections were performed by adding +0.5 mm to SGP (**SC**) or by adding the values that were estimated with linear approximation ($0.02728 \times \text{SGP} - 0.4178$) to SGP (**SL**). To increase the number of SGP data, the SGP obtained at -30 min and -15 min before the hour (00 min) were also assimilated in cases of **SN3**, **SC3** and **SL3**. In these cases, the SGP data at -30 min and -15 min before the hour were not used when the vessels were not moving.

4. Assimilation results of shipborne GNSS

The results of **CNTL**, **SC3** and **SL3** are shown in fig.

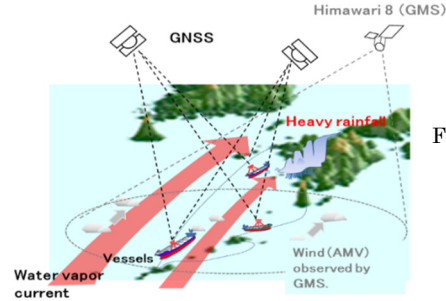


Fig. 1 Illustration of data assimilation experiments for shipborne GNSS observation.

2. The intense rainfall regions where 3-hour amounts exceeded 50 mm were observed over the northern Kyushu (indicated by a red circle in fig. 2a). Figure 2b shows the 3-hour rainfalls that were predicted in different experiments. The intense rainfalls were well reproduced in **SC3** and **SL3**, while they were not seen in the northern Kyushu in **CNTL**. In **SL3**, in the region extending to southwest from the northern Kyushu, the rainfall was too intense, compared with observations. This rainfall was caused by the larger PWV on the west of Kyushu (blue arrow).

The differences of PWV predicted in **CNTL** and **SC3**, **SL3** at the forecast times (FTs) from 1 to 3 hours are shown in fig. 2c. The regions with increased PWV (red regions) that were produced by the assimilation of SGP moved northeast (indicated by red arrows) and then it led to the intense rainfalls (thin black lines, 20 mm). As for the PWV-increased regions on the south of Kyushu (black arrows), they disappeared when the linear approximation was adopted (**SL3**).

The impact of the number of SGP data was shown by the extended forecasts at FTs from 3 to 9 hours (fig. 3). The intense rainfalls (indicated by red arrows) were reproduced only in **SN3**, **SC3** and **SL3** at FTs=3 and 6, though the rainfall extending to southwest were too intense in **SN3** and **SL3**, and the intense rainfalls were reproduced at FT=9 in all cases. This result suggests that the number of vessels that provide SGP data should be increased to improve the accuracy of rainfall forecasts.

Table 1. Data assimilation experiments of shipborne GNSS

Case	SGP	Bias correction	Time of assimilation
CNTL	No	-	-
SN	Yes	+0.0 mm	00 min
SC	Yes	+0.5 mm	00 min
SL	Yes	Linear approx.	00 min
SN3	Yes	+0.0 mm	-30, -15, 00 min
SC3	Yes	+0.5 mm	-30, -15, 00 min
SL3	Yes	Linear approx.	-30, -15, 00 min

5. Summary

The results of this report indicate that SGP data should be considered as useful for data assimilation and that the increase of the number of SGP observations improves the rainfall forecast. The further studies on

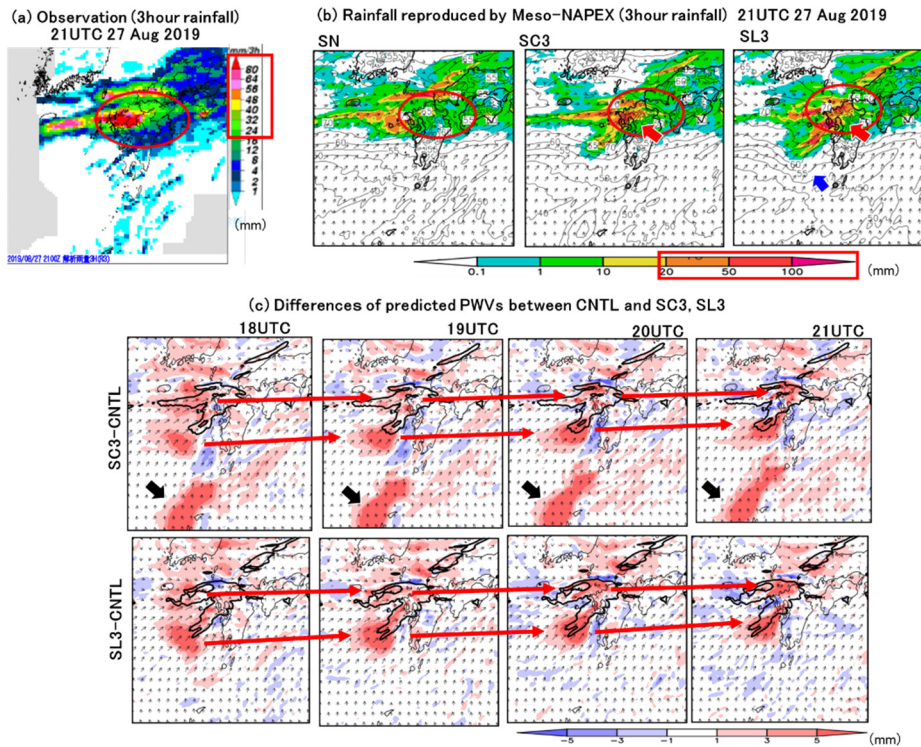


Fig. 2 (a) Observed 3-hour rainfall distribution at 21 UTC 27th Aug. 2019. (b) Rainfall distributions of 3-hour forecasts at 21UTC that were obtained in **CNTL**, **SC3**, and **SL3**. (c) Differences of the predicted PWV between **CNTL**, **SC3**, and **SL3**.

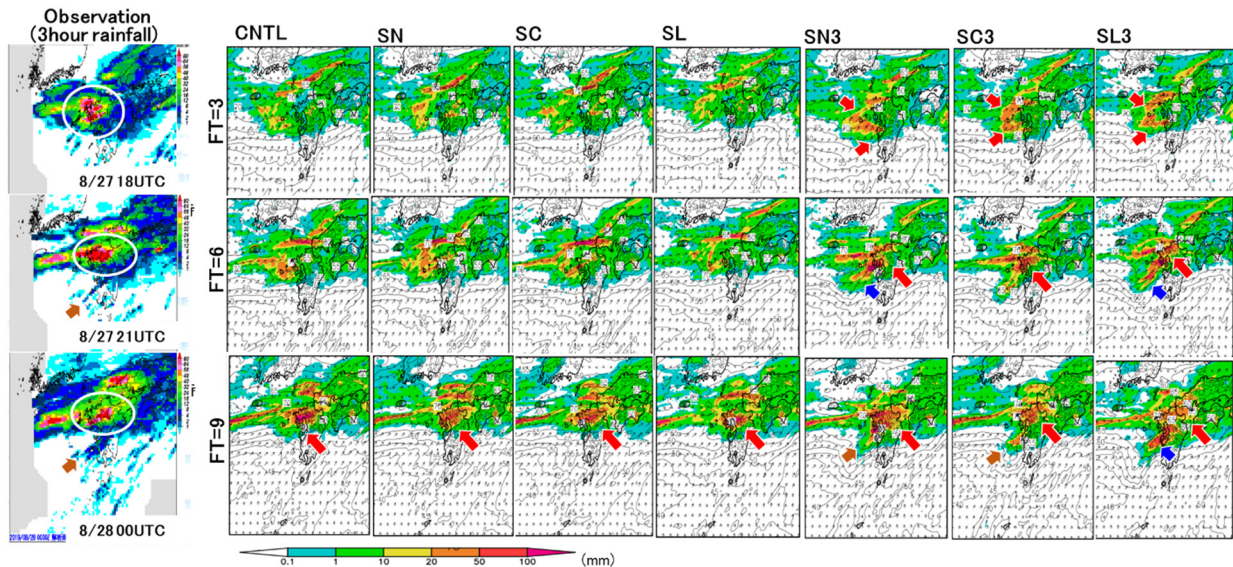


Fig. 3: 3-hour rainfall distributions of the extended forecasts, in which the start time of data assimilation was changed from 18UTC to 15UTC 27th Aug 2019.

the bias correction and of the synergy effect of wind data are desired.

Acknowledgments

The study was partly supported by Grant-in-Aid for Scientific Research (S) 'A challenge to the high functionality of Tsunami observation and the continuous observation of crustal movement at sea floor using the marine GNSS buoy'.

References

Seko, H., K. Koizumi, and Y. Shoji, 2019: Impact of data assimilation of shipborne GNSS data on rainfall forecast. *CAS/JSC WGNE Research Activities in Atmospheric and Oceanic Modelling/WMO*. **49**, 1-23

Shoji, Y., K. Sato, M. Yabuki, and T. Tsuda, 2017: Comparison of shipborne GNSS-derived precipitable water vapor with radiosonde in the western North Pacific and in the seas adjacent to Japan. *Earth Planets Space*. **69**, 153.

Shoji, Y., T. Tsuda, T. Kato, T. Terada, and M. Yabuki, Ocean Platform GNSS Meteorology for Heavy Rainfall Prediction, Living Planet Symposium 2019, 2019, May, Italy, Milan.

Implementation of all-sky microwave radiance assimilation into JMA's global NWP system

SHIMIZU Hiroyuki, KAZUMORI Masahiro and KADOWAKI Takashi

Numerical Prediction Division, Japan Meteorological Agency

E-mail: shimizu_h@met.kishou.go.jp

1. Introduction

Microwave radiance data from space-based observation contain a variety of information on geophysical parameters relating to the atmosphere and the earth's surface (e.g., atmospheric temperature, water vapor, cloud, precipitation, surface wind and surface temperature). In this context, microwave radiance over ocean areas in clear-sky conditions has been assimilated in JMA's global numerical weather prediction (NWP) system since May 2003 (Okamoto et al., 2005). As microwave radiance data relating to cloud and precipitation contain information on the presence of water/ice particles, assimilation of all-sky (including clear-sky, cloud and precipitation) microwave radiance contributes to better forecasting of atmospheric phenomena associated with severe weather conditions. The tracing effect of such assimilation based on 4D-Var also helps to improve dynamical initial conditions and supports improved forecasting (Geer et al. 2014).

JMA developed an all-sky microwave radiance assimilation scheme for microwave imagers and microwave water-vapor sounders (Kazumori and Kadowaki, 2017), including outer-loop iterations for trajectory updates in the 4D-Var minimization process for effective assimilation of cloud and precipitation. It was introduced into JMA's operational global NWP system in December 2019. This report gives an overview of all-sky microwave radiance assimilation.

2. Data and Quality Control

The RTTOV-SCATT (Radiative Transfer for TOVS; Bauer et al., 2006) model enables multiple-scattering radiative transfer calculation for microwave frequencies as part of the RTTOV-10 package adopted as an observation operator for all-sky assimilation processing. Observation error assignment based on the symmetric (average of observation and first guess (FG)) cloud amount (Geer and Bauer, 2011) is applied to handle the non-Gaussian distribution of observation errors. Biased data such as those caused by insufficient cloud representation in JMA's global forecast model (e.g., cold-sector bias) are removed, as the related observation error cannot be treated appropriately even if observation errors based on the symmetric cloud amount are considered. The all-sky assimilation scheme is applied to microwave imager (AMSR2/GCOM-W, GMI/GPM, SSMIS/DMSP F-17, F-18) and microwave water-vapor sounder (GMI/GPM, MHS/NOAA-19, Metop-A, -B) data previously assimilated under clear-sky conditions. Two additional microwave sensors (WindSat/Coriolis, MWRI/FY-3C) that had not been utilized in JMA's global NWP system were also included in all-sky assimilation.

3. Impact Evaluation: Data Assimilation Experiments

Data assimilation experiments were conducted using JMA's global NWP system for the period from November 2017 to March 2018 (winter) and June to October 2018 (summer). The CNTL experiment had the same configuration as JMA's operational global NWP system as of December 2018, and the TEST experiment represented all-sky assimilation for microwave imagers and microwave water-vapor sounders with two outer-loop iterations for trajectory updates in the 4D-Var minimization process.

Figure 1 shows differences in the standard deviations of FG departure statistics and the number of used data about SAPHIR/Megha-Tropiques (Sondeur Atmospherique du Profil d'Humidite Intertropicale par Radiometrie; only shown at 183.31 ± 11 GHz; sensitive to lower-tropospheric water vapor) whose data are assimilated under clear-sky conditions for both experiments. The number of SAPHIR data used in TEST was higher, and the standard deviations for FG departure were lower. These results indicate improved FG water vapor fields in TEST for the lower troposphere in the tropics.

Figure 2 shows the improvement ratio for the root mean square error (RMSE) of geopotential height at 500 hPa verified against the experiments' own analysis. Improvement was observed for most of the forecast range up to 120 hours in the summer and winter experiments, and other elements (e.g., sea level pressure and wind speed at 850 hPa) also exhibited improvement (not shown).

Figure 3 shows average TC track forecast errors and differences between TEST and CNTL for the summer and winter experiments. Errors in TEST decreased over the whole forecast range up to 96 hours with statistical significance for the forecast range up to 72 hours.

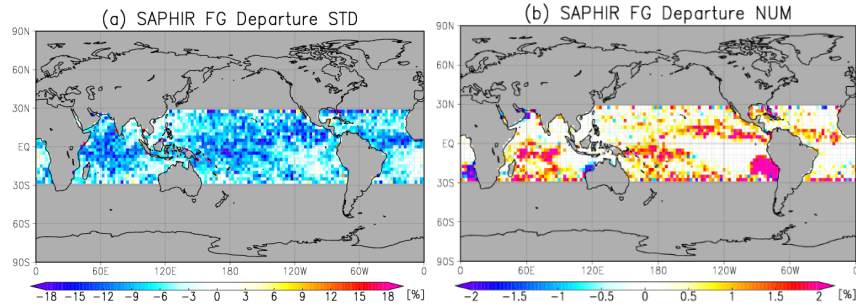


Figure 1: (a) Normalized changes for SAPHIR (brightness temperature [K] at 183.31 ± 11 GHz) standard deviations of FG departures and (b) ratio of number of data used [%].

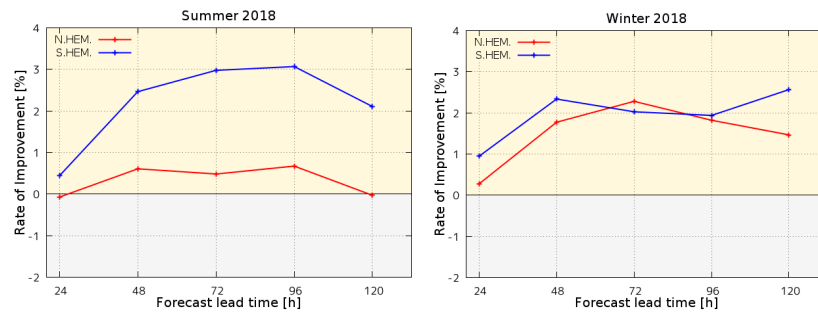


Figure 2: Improvement ratio $((\text{CNTL} - \text{TEST}) / \text{CNTL})$ [%] for the RMSE of geopotential height at 500 hPa verified against the experiment's own analysis. Positive values indicate forecast error reductions of TEST against CNTL. The figures on the left and right show results for summer and winter 2018, respectively. The red and blue lines show verification results for the Northern Hemisphere ($20 - 90^\circ\text{N}$) and the Southern Hemisphere ($20 - 90^\circ\text{S}$), respectively.

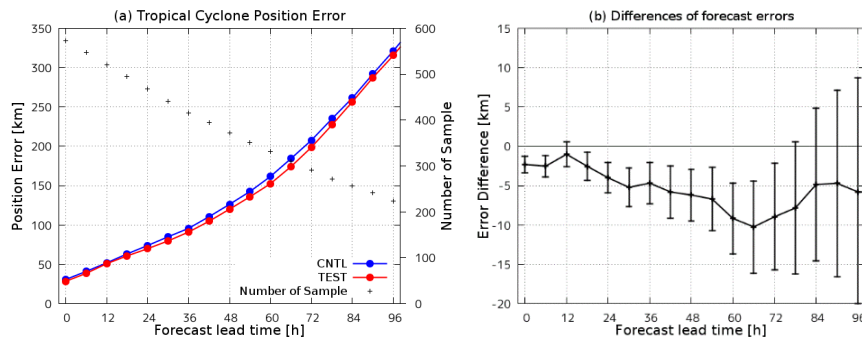


Figure 3: (a) Average TC track forecast errors for the summer and winter experiments. The red and blue lines are for TEST and CNTL, respectively, and dots represent sample data numbers. (b) Forecast error differences between TEST and CNTL. Error bars represent a 95% confidence interval.

References

- Bauer, P., E. Moreau, F. Chevallier, and U. O'Keeffe, 2006: Multiple-scattering microwave radiative transfer for data assimilation applications. *Quart. J. Roy. Meteorol. Soc.* **132**, 1259-1281
- Geer, A. J., F. Baordo, N. Bormann and S. J. English, 2014: All-sky assimilation of microwave humidity sounders. *ECMWF Tech. Memo.*, 741, available from <http://www.ecmwf.int>.
- Geer, A. J. and P. Bauer, 2011: Observation errors in all-sky data assimilation. *Quart. J. Roy. Meteorol. Soc.* **137**, 2024-2037
- Kazumori, M., T. Kadowaki, 2017: Development of an all-sky assimilation of microwave imager and sounder radiances for the Japan Meteorological Agency global numerical weather prediction system. *Tech. Proc. of 21st International TOVS Study Conference, Darmstadt, Germany 29 November – 5 December 2017*.
- Okamoto, K., M. Kazumori, and H. Owada, 2005: The assimilation of ATOVS radiances in the JMA global analysis system. *J. Meteor. Soc. Japan.* **83**, 201-217.